Enhanced structural, optical, electrochemical and magnetic behavior on manganese doped tin oxide nanoparticles via chemical precipitation method

S. Sivakumar[1] · E. Manikandan[1]

Abstract

A series of $Sn_{1-x}Mn_xO_2$ (X = 0.00, 0.015, 0.025, 0.035 and 0.045 mol%) nanoparticles have been synthesized by effective chemical precipitation method. In this work to explore the structural, morphological, optical, electrochemical and magnetic properties of the pure and Manganese doped SnO_2 nanoparticles are characterized on the TG/DTA, XRD, SEM/EDX, HR-TEM, FTIR, UV–DRS, PL, CV, and VSM analysis. XRD indicates that the tetragonal crystal structure, with the crystallite size of range from 37 to 11 nm. The structure, size, shape, and morphology analysis by SEM and HR-TEM was spherical shape is observed. FTIR studies on functional group analysis of pure and Manganese doped SnO_2 nanoparticles. The peak appeared at 619 cm^{-1} due to O–Sn–O stretching vibration of clearly indicates the formation of SnO_2 phase. UV–DRS absorption measures were the optical band gap energies decreasing with increasing Mn (0.00%, 0.015%, 0.025%, 0.035% and 0.045%) concentration from 3.89 to 3.75 eV. UV–DRS analyzed the mechanisms of electron–hole recombination and charge carriers separation. Further, the electrochemical properties were subsequently characterized by cyclic voltammetry. From the CV performance of the supercapacitor application was analyzed, the higher capacitance value of pure and Manganese (0.045%) doped SnO_2 electrode 156.7 Fg^{-1} and 285.2 Fg^{-1} observed in the scan rate of 5 mV s^{-1} for the product calcinated at 700 °C. The M–H loop of pure SnO_2 nanoparticles showed diamagnetism, Manganese doped SnO_2 nanoparticles show weak ferromagnetic and paramagnetic behavior at room temperature as measured by VSM. A tin oxide with lower manganese concentration show larger magnetization and with increasing manganese concentration the retentivity and coercivity are found to decrease. The magnetic parameters such as saturation magnetization (M_S), coercivity (H_C) and retentivity (M_R) are obtained from VSM data.

1 Introduction

Synthesis and characterization of nanomaterials are gaining recognition among the scientific communities for fundamental or applied research because many material properties change significantly as the particle size reaches the nanometer assortment. Nanoscale has been looked into broadly for their fashionable size-dependent properties, such as electricity, optics, and magnetism [1–3]. From the various metal oxides, SnO_2 materials such formation of a tetragonal structure is an important role of n-type band gap energy (3.6 eV at RT). Due to the band gap energy the semiconductors that are various distinctive properties such as chemical, optical and electronic, such as owing to catalysis, solar cells, gas-sensing, spintronics [4–7] and portable electronic [8] device applications due to its high electric conductivity (21.1 Ω cm), high theoretical capacity, as well as superior electron mobility (100–200 cm^2/Vs). In addition, tin oxide, also well known capable candidates for diluted magnetic semiconducting materials, while the transition metal 3d ions for impurities were replaced into the cation site of ZnO nanoparticles [9]. Thus, the final properties of impurity doped SnO_2 nanoparticles are developed for numerous applications in magnetic, electrical and optical devices, manganese nanoparticle can be a respectable possibility to supplant Sn particle in the SnO_2 cross section since its unrivaled warm dissolvability (10 mol%), it can expand the measure of infused twists and bearers [10]. While various

✉ S. Sivakumar
girihari777@yahoo.com

E. Manikandan
e.mani16041992@gmail.com

[1] Department of Physics, Annamalai University, Annamalainagar, Tamil Nadu 608002, India

test examines the attraction of SnO_2 based DMSs doped with progress metal (TM, for example, Co, Mn, Fe, Ni, and Cr) [11–15], disputable outcomes have reported on magnetism prepared by various techniques and researchers. With esteemed Manganese doped SnO_2, announced ferromagnetism over room temperature in bulk product [13, 16]. Observed ferromagnetism only below 27 K for $Sn_{1-x}Mn_xO_2$ (x = 0.01, 0.03, 0.05) bulk counterpart was prepared using a solid-state method [17]. Nanosized doped SnO_2 have been synthesized by various techniques such as simple chemical co-precipitation method [18], sol–gel method [13], and early techniques were reported.

In the era, we complete an effort to study the effect of the thermal behavior, structural analysis, functional analysis, morphology and elemental analysis, optical and energy band gap, electrochemical and magnetic properties of the synthesized products of pure and manganese doped SnO_2 nanoparticles were reported through TG/DTA, XRD, FTIR Spectroscopy, SEM, HR-TEM, UV–DRS, CV and VSM.

2 Synthesis procedure

2.1 Materials

All the chemicals were purchased by Sigma Aldrich AR grade. Aqueous solutions containing stoichiometries rates of the precursors for tin(IV) chloride pentahydrate ($SnCl_4 \cdot 5H_2O$), manganese(II) chloride tetrahydrate ($MnCl_2 \cdot 4H_2O$) and, distilled water was used in the following synthesis process.
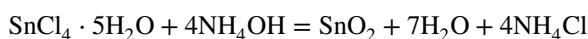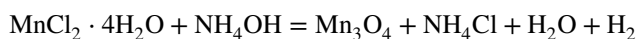
2.2 Synthesis of SnO_2 nanoparticles

In synthesis process, several concentrations of 0.015%, 0.025%, 0.035% and 0.045% Manganese-doped and pure SnO_2 nanoparticles were synthesized by chemical precipitation technique. A transparent solution was synthesized by controlling the mixing of 0.1 M $SnCl_4 \cdot 5H_2O$ was dissolved 100 ml distilled water. After a few minutes stirring and the precipitation was obtained by adding a sufficient amount of NH_4OH to the above transparent solution. The resulting precipitation was filtered and washed, with distilled water and used absolute ethanol to remove the impurities, the final products were dried at 80 °C for hot air oven, and it was further calcined at 700 °C for 2 h to maintain a furnace. A comparative strategy was taken after for the planning of the Manganese doped SnO_2 nanoparticles, with the assistance of manganese chloride to the transparent tin(IV) chloride arrangement sooner than the expansion of NH_4OH and the convergence of the Manganese was changed in the concentration of 0.015–0.045 mol%.
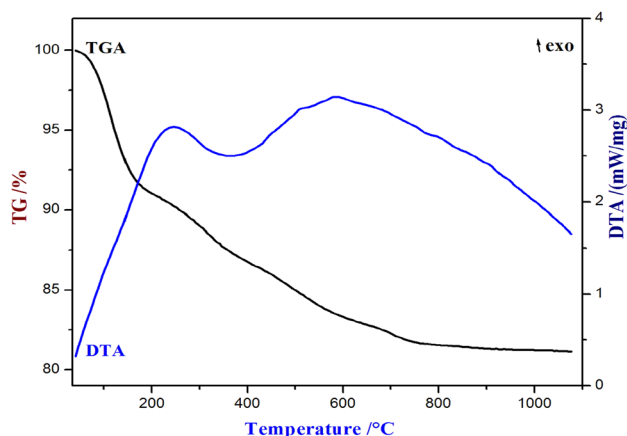
2.3 Characterization of SnO_2 nanoparticles

The phase confirmation of the pure and Manganese doped SnO_2 nanoparticles was characterized in X-ray diffraction technique using PW3040/60 X'pert PRO powder X-ray diffractometer with CuKα radiation (λ = 1.5406 Å) at 40 kV and 30 mA. The scans for two theta range from 20° to 80° available at Alagappa University, Karaikudi, Tamilnadu, India. TG/DTA investigation utilized the instrument NETZSCH-STA 449 F3 JUPITER available at Instrumentation and Services Laboratory (CISL), Annamalai University, Annamalai Nagar, Tamilnadu, India. SEM was well known for utilizing a scanning electron microscope, EVO18 MODEL available at St. Joseph's College, Tiruchirappalli, Tamilnadu, India. The analysis of morphology was done by HR-TEM using JEM 2100 F, available at SAIF, Cochin and Kerala, India. UV–DRS spectroscopy using SHIMADZU-UV 2600 spectrometer available at dept. of Chemistry Annamalai University, Annamalainagar, Tamilnadu, India. The Photoluminescence were measured in a make Jobin Yvon, model FLUOROLOG-FL3-11 available at CIF, Pondicherry University, Puducherry. The electrochemical property of the nanoparticles was carried out by cyclic voltammetry using model CHI 660 available at St. Joseph's College, Tiruchirappalli, Tamilnadu, India. The magnetic behaviors were analyzed in make lakeshore, model 7410 series at room temperature available at CIF, IIT Guwahati, Guwahati.

3 Results and discussions

It is better to identify that tin hydroxide begins to form at pH 0.5 [19]. In addition, Sn(IV) has a tendency to hydrolyze in the fluid solution, shaping charged and uncharged types of $SnO(OH)_3$ at pH 8 and $SnO(OH)_2$ at pH 7, respectively [20]. Identified with respectively. $SnO(OH)_2$ was first formed in the present investigation at pH 8 [20], But, Seby et al., was unable to explain the complete studies. We carried out the present study and try to give the complete pieces of information about SnO_2 nanoparticles. Further reported that dopants are shaped as they hydroxides on the surface of $SnO(OH)_2$ particles [19]. In addition, Manganese hydroxide was formed at pH 7 as $Mn(OH)_2$ on the surface of $SnO(OH)_2$ particles during the precipitation. At that point, they were changed into their relating oxides along with the calcination procedure [19]. On the following chemical reaction is given by:

$$MnCl_2 \cdot 4H_2O + NH_4OH = Mn_3O_4 + NH_4Cl + H_2O + H_2$$

$$SnCl_4 \cdot 5H_2O + 4NH_4OH = SnO_2 + 7H_2O + 4NH_4Cl$$

$Mn(OH)_2$ existing on the surface of SnO_2 was transformed into their corresponding oxides. Obviously, a few

Fig. 1 Thermogravimetric and differential thermal analysis plot of SnO_2 as-prepared sample

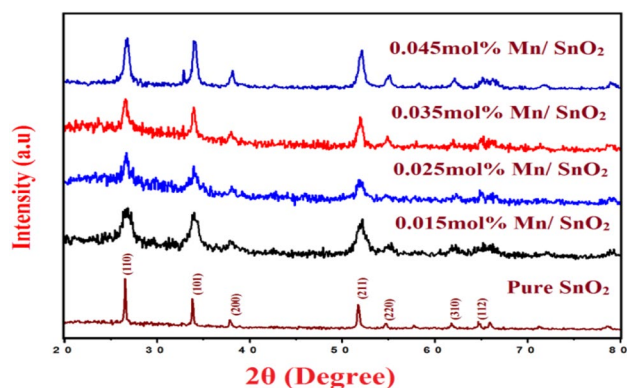**Fig. 2** X-ray diffraction of pure and Manganese doped SnO_2 nanoparticles calcinated at 700 °C

cations were required to be moved into the inside of SnO_2 and form a solid solution [19, 21].

3.1 TG/DTA studies

The thermal behavior of the as-synthesized tin oxide sample as shown in Fig. 1. A thermal property of the synthesized product was deliberated by differential thermal analysis (DTA) and thermogravimetry (TG) analysis. The differential thermal analysis, curve showed the endothermic peak at 420 °C, which confirms the decomposition of hydroxide, and exothermic peaks appeared at 275 °C is the removal of hydroxide. This may be related to the decomposition of precursor $SnCl_4 \cdot 5H_2O$ at 420 °C and 590 °C with an elimination of the nitrates [22]. These occur in involving that intra and inter-molecular transfer reaction. The thermogravimetry curve predicts three major weight loss regions. The first step, from room temperature to 180 °C due to 9% of weight loss is occurred, which is caused by dehydration and evaporation of alcohol existing in the product. The second step, 180–580 °C for the weight loss is about 7%, which is accredited to the removal of the strongly bound water or the surface hydroxyl groups present in the product. The final step, 580–700 °C for weight loss is about 3%, which results from the decomposition of the remained ammonium chloride. The complete weight loss value upon heating to 1100 °C was about 19%. No other weight loss in TG was observed at 700 °C achieving the stable phase of the material [23].

3.2 XRD studies

The X-ray diffraction of $Sn_{1-x}Mn_xO_2$ nanoparticles was calcined at 700 °C in Fig. 2. The phase identification of pure and manganese doped SnO_2 nanoparticles with the composition (0.015, 0.025, 0.035 and 0.045 mol%) is characterized

by X-ray diffractometer. All the diffraction peaks reflect (110), (101), (210), (211), and (112) planes confirmed that the synthesized nanoparticles possess a tetragonal structure [24] with p42/mnm space group. The peaks present in the obtained XRD patterns are well matched with compared to JCPDS card no. 77-0449 and it's confirmed that the synthesized pure and manganese doped SnO_2 nanoparticles [25]. The average crystallite size is measured by Debye Scherrer's equation [26].

$$D = \frac{k\lambda}{\beta \cos \theta} \tag{1}$$

where D is the crystallite size of tin oxide nanoparticles, k is the Scherrer constant with the value from 0.89 to 1 and θ is the Bragg's angle, λ is the wavelength of X-ray source (0.1546 nm), and β is known as the FWHM of the diffraction pattern. The Table 1 shows that all structural parameters were calculated. The average crystallite size of the pure SnO_2 nanoparticles size is 37 nm and the manganese doped SnO_2 nanoparticles average crystallite size ranging from 23 to 11 nm. The manganese concentration increased from 0.015 to 0.045 M% with the crystalline decreased from 23 to 11 nm. Further, the structural parameters such as dislocation density (δ), microstrain (ε) and unit cell volume (V) were also determined from the XRD data by the following equations [27, 28].

$$\delta = \frac{1}{D^2} \tag{2}$$

$$\varepsilon = \frac{\beta \cos \theta}{4} \tag{3}$$

$$V = a^2 c \tag{4}$$

If all the above-mentioned factors were minimum, then the crystallinity of the prepared product should be better. It

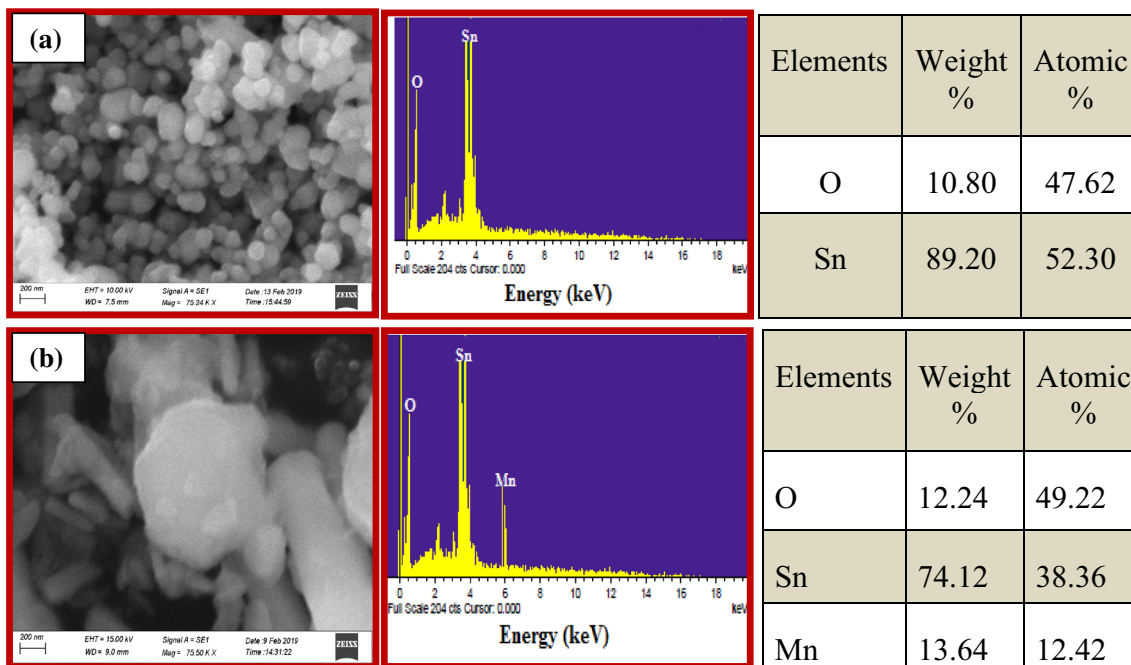**Table 1** Various structural parameters calculated from the XRD pattern

Samples	Lattice parameter		Unit cell volume (V)	Dislocation density (δ)	Micro strain (ε)	Average crystallite size (D)	Bandgap energy (eV)
	a = b	c					
Pure SnO_2	4.7477	3.1945	72.0061	0.0007	0.0359	37	3.89
Mn 0.015%	4.7502	3.1913	72.0097	0.0082	0.1196	23	3.75
Mn 0.025%	4.7434	3.1748	71.4325	0.0044	0.0957	17	3.67
Mn 0.035%	4.7323	3.1721	71.0381	0.0034	0.0957	15	3.62
Mn 0.045%	4.7237	3.1682	70.6931	0.0018	0.0718	11	3.52

is evident from Table 1 indicate that the values of dislocation density (δ), microstrain (ε) and unit cell volume (V) were calculated and these values given the information about the high crystallinity of synthesized manganese doped SnO_2 nanoparticles. Some researchers also observed a reduction in the crystallite size with an increase in the manganese content [29]. In general, as the increasing manganese concentration such as (0.015, 0.025, 0.035 and 0.045 M %) the peak intensity increases. Whereas decreases lattice parameter it may be due to the fact of Manganese ions are inclined to incorporate into the lattice in the form of Mn^{3+} (0.65 Å) ions or Mn^{4+} (0.54 Å) since their ionic radius is smaller that of Sn^{4+} (0.69 Å). It's obeying the mechanism of Vegard's law [30].

3.3 Morphology analysis

The morphology of pure and manganese doped SnO_2 (0.045%) nanoparticles have been characterized by the means of SEM images in Fig. 3. It is observed that the particles are spherical in shape on the surface [31]. The EDX spectrum of pure SnO_2 and manganese doped SnO_2 (0.045%) nanoparticles calcined at 700 °C as shown in Fig. 3. From EDX spectra of the element present in the pure SnO_2 product are identified as Sn and O are major trace elements, and manganese doped SnO_2 product are identified Mn, Sn, and O are major trace elements. These results suggest that the pure SnO_2 and manganese doped SnO_2 (0.045%) nanoparticles calcined at 700 °C have been formed. In addition, the atomic/weight percentage was listed. Figure 4 shows that the HR-TEM picture of the pure and manganese doped SnO_2 (0.045%) nanoparticles. The spherical morphology is well dispersed, the few aggregated particles were observed in an HR-TEM picture. The corresponding average particle size was calculated at 36.8 nm and 12.0 nm, these are a good result with the size that has been estimated from the XRD and confirm that

Elements	Weight %	Atomic %
O	10.80	47.62
Sn	89.20	52.30

Elements	Weight %	Atomic %
O	12.24	49.22
Sn	74.12	38.36
Mn	13.64	12.42

Fig. 3 SEM images of **a** pure and **b** Manganese (0.045 mol%) doped SnO_2 nanoparticles corresponding EDAX spectrum and weight percentage
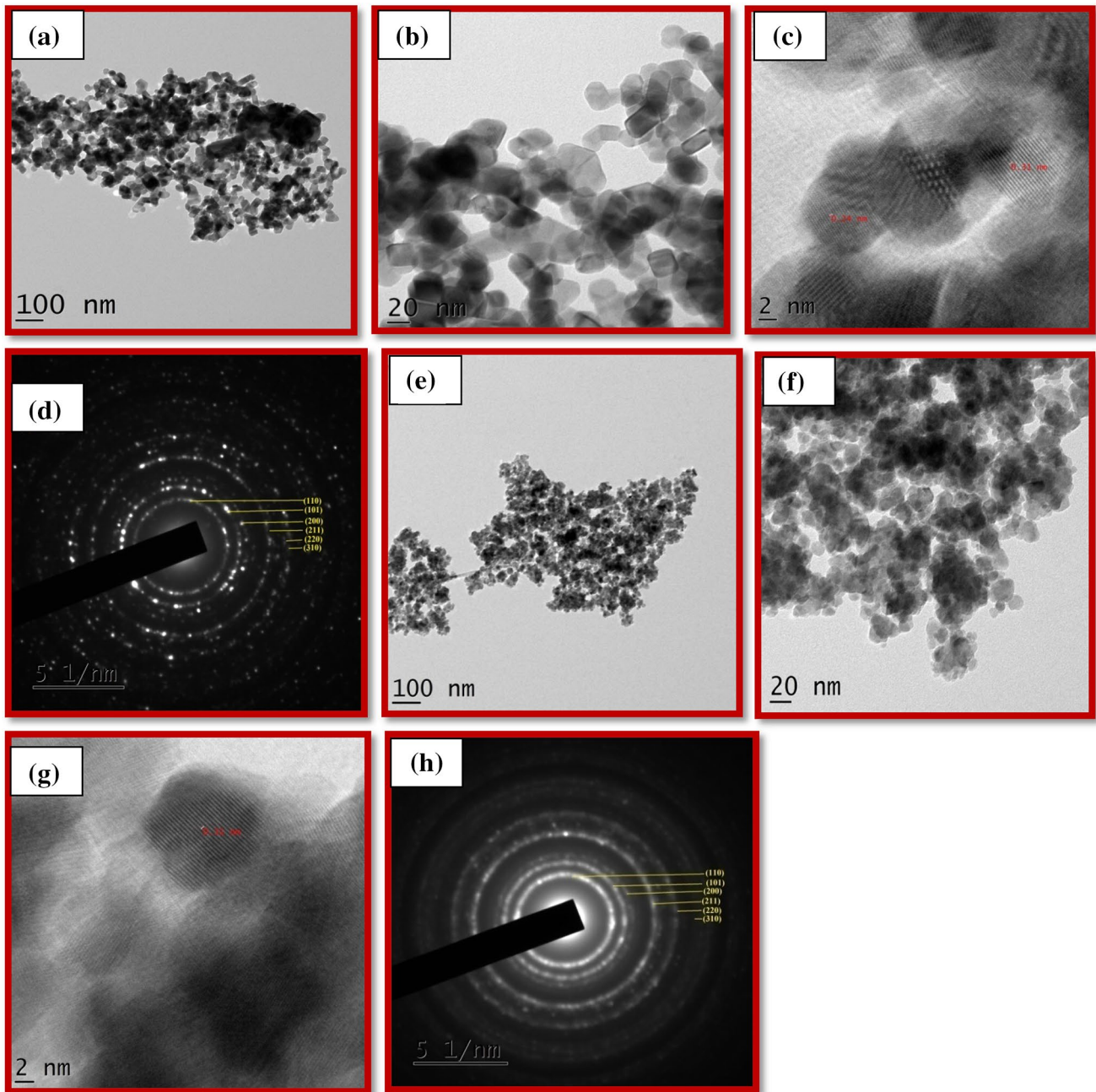
Fig. 4 **a–c, e–g** HR-TEM images of pure and Manganese (0.045%) doped SnO$_2$ nanoparticles. **d, h** Corresponding SAED pattern of pure and Mn (0.045%) doped SnO$_2$ nanoparticles

the reduction in particle size is the result of increasing the manganese concentrations [32]. Also, the corresponding to the polycrystalline rings exhibited on SAED pattern, which were all from the rutile tetragonal structure of SnO$_2$, is shown in Fig. 4. These rings indicate the well crystalline nature of the sample is shown in XRD spectra (Fig. 2). The metal ions doped SnO$_2$ nanoparticles prepared to use a chemical precipitation process are alike in size mutually

narrow size distribution and are readily dispersed [33]. It shows that the crystallinity increases with an increase in manganese content of 0.045%. The graphical size distribution histogram presented in Fig. 5, which is obtained from the micrograph from the image of pure and manganese (0.045%) doped SnO$_2$ nanoparticles and get in average particle size is 36.8–12.0 nm respectively, with the help of image J viewer Software.
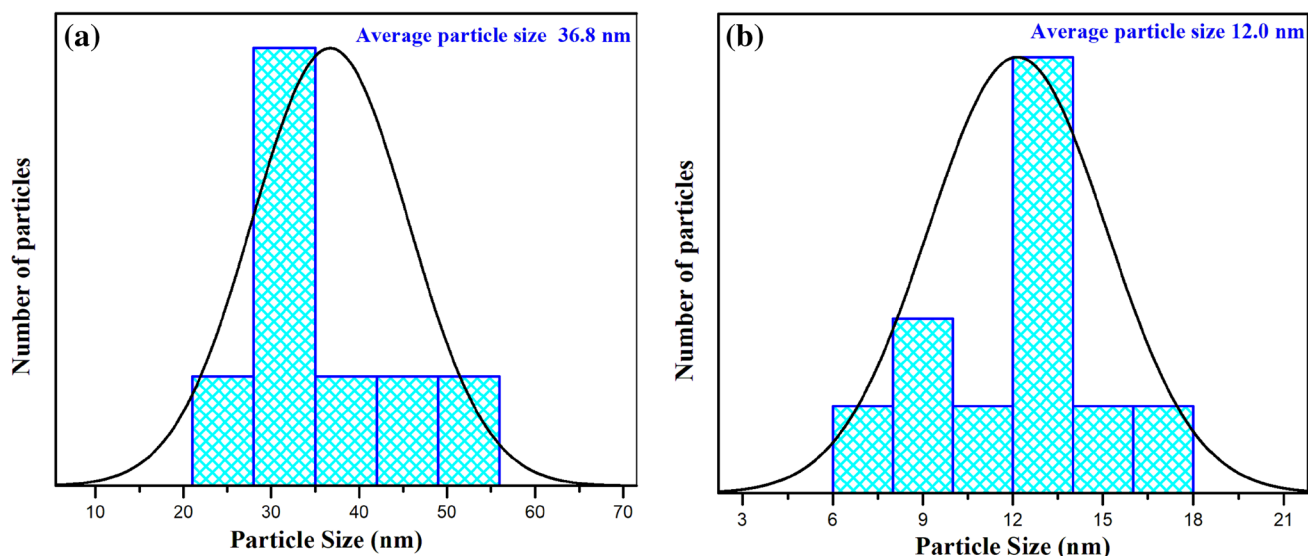
Fig. 5 Particle size distribution graphs for **a** pure and **b** Manganese (0.045%) doped SnO$_2$ nanoparticles
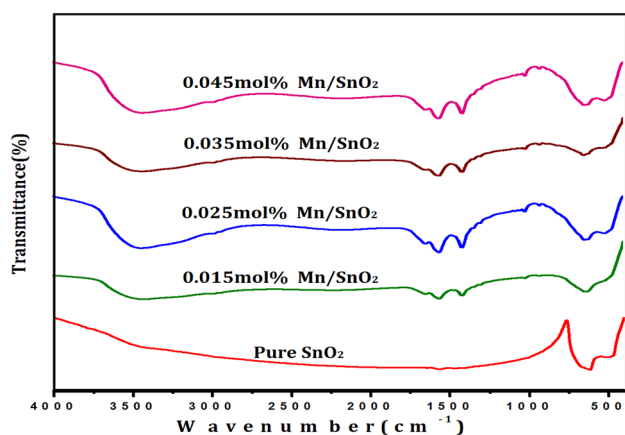
Fig. 6 FTIR spectra for pure and Manganese doped SnO$_2$ nanoparticles at different concentration cacinated at 700 °C

3.4 FTIR studies

The FTIR spectra Fig. 6 show that the SnO$_2$ and the manganese doped SnO$_2$ nanoparticles (0.015%, 0.025%, 0.035% and 0.045%). KBr pellet techniques were using for recorded on FTIR spectra in the range of wavelength is 4000–400 cm^{-1}. The observed stretching vibration band at 619 cm^{-1} to the Sn–O–Sn antisymmetric stretching mode can be assigned. The band region on 470 and 517 cm^{-1} can be accredited to symmetric bonds Sn–O–Sn and Mn–O respectively [29–34]. The vibration band observed at 1471 cm^{-1} can be assigned to the symmetrical stretching N–O for the existence of nitrogen-based compounds due to the synthesis of nitrate precursors in the product, while the peak at 1765 cm^{-1} is assigned to C=O is stretching vibration. The present assignments support the values reported in the available literature [24, 35]. The peak appeared in 619, 642, 644, 648 and 650 cm^{-1} in all products are due to O–Sn–O bridge functional group which clearly indicates the formation of SnO$_2$ phase [36]. It has been attributed that, the increase in manganese content causes the small shift in wavenumber to the lower region.

3.5 UV–DRS studies

Figure 7 shows that the optical properties of manganese doped SnO$_2$ nanopowders were analyzed by UV–DRS spectrum. The sketch plotted [F (R∞) hυ] versus hυ shows that intercept value and the band gap energy of 3.89 eV [37] during the extra plotting as shown in Fig. 7. It can exist in the band gap energy of 3.89 eV, considered that the spectra of manganese doped SnO$_2$ show that massive blue shift in the band gap transition with doping manganese elements. The band gap value for pure SnO$_2$ is 3.89 eV, which is in good agreement with the reported values [38]. The manganese doped SnO$_2$ product display with the increase in the doping concentrations, the band gap value has drastically decreased from 3.75 to 3.52 eV, the noted reduce in band gap energy can be about the charge transfer during the manganese ions and SnO$_2$ conduction or valence band. It can be inferred from reducing in the optical band gap that manganese ions have been included in Sn sites of SnO$_2$ lattice homogeneously.
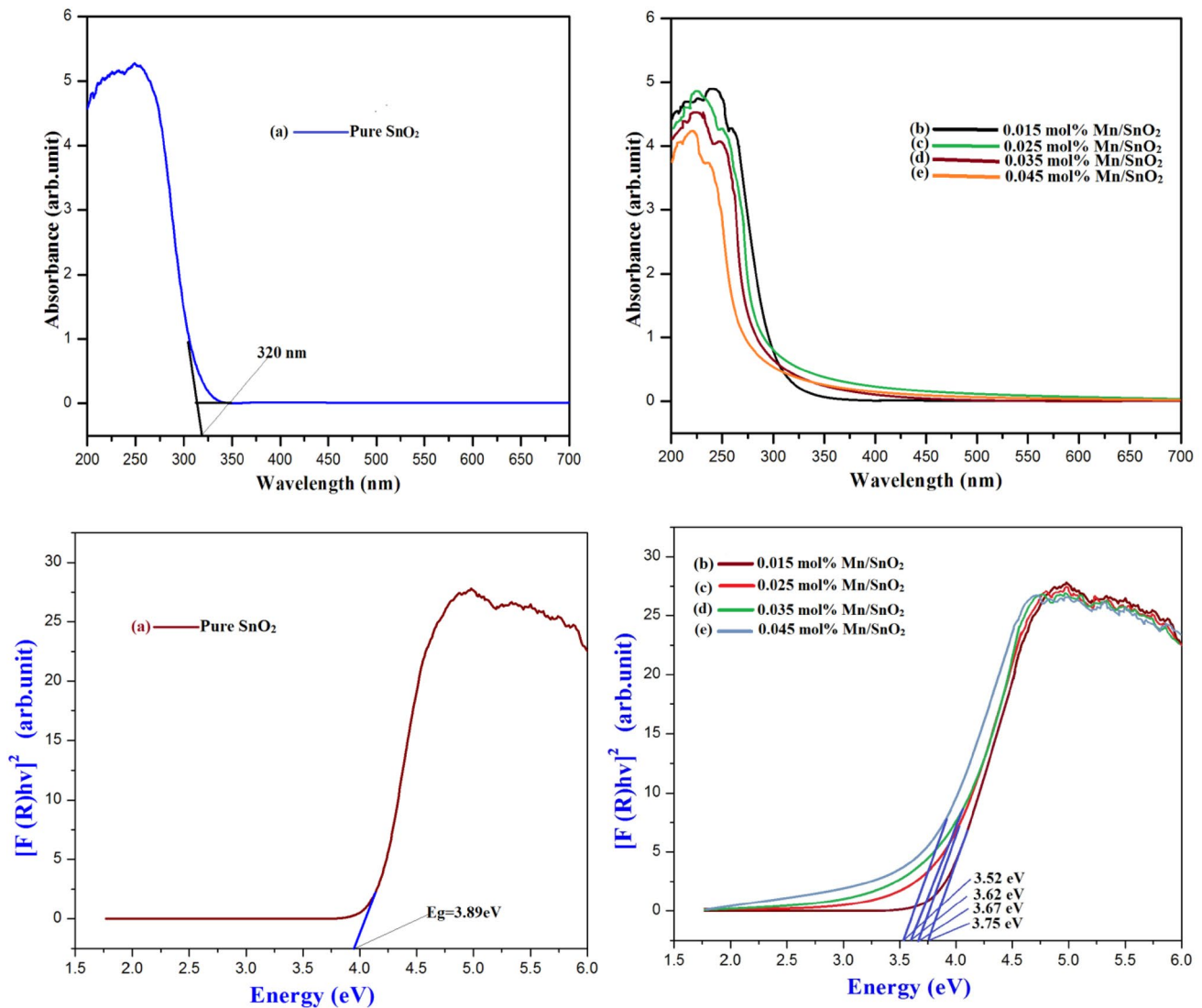
Fig. 7 Kubelka–Munk plots for direct band gap determination of the (a) Pure SnO_2 nanoparticles (b) 0.015 M% (c) 0.025 M% (d) 0.035 M% and (e) 0.045 M% Manganese doped SnO_2 nanoparticles

3.6 Photoluminescence studies

The room temperature PL emission spectra of manganese doped SnO_2 nanoparticles are exposed in Fig. 8. An excitation wavelength of 320 nm indicates the clear UV emission bands. Likewise, the observed in a strong visible emission peak at 425 nm can be assigned to the luminescent centers in the SnO_2 nanoparticles. In addition, the various weak emission peaks showing at 445, 467 and 538 nm are reasonable to have started from the oxygen vacancies [39]. Furthermore, it can be seen that the manganese concentrations increase with the intensity of luminescent emission increases, which possibly because of the increase in the oxygen vacancies as a role of the manganese concentrations. Also, some works of literature have previously said that smaller sized nanoparticles

have a higher population of surface defects for the enhanced defect emission applicable to the UV emission, as seen in the appearance of metal ion doped metal oxide nanoparticles [40, 41]. The oxygen vacancies are present in three different charge states V_o^0, V_o^+, and V_o^{2+} in the oxide. As a very shallow donor is V_o^0, the majority oxygen vacancies will be in their paramagnetic V_o^+ state under flat band conditions. The peaks might too come from the luminescence centre of tin interstitials or dangling etc. in the pure and manganese doped SnO_2 nanoparticles. The previous reports recommended that the broad peaks around 400–500 nm can be assumed to be due to the formation of a V_o^{++} luminescent centre in the SnO_2 nanocrystals and nanorod [42].

In this case of doped samples, it is easy for Mn^{2+} ions to substitute for Sn^{4+} ions because the nearly same ionic radius
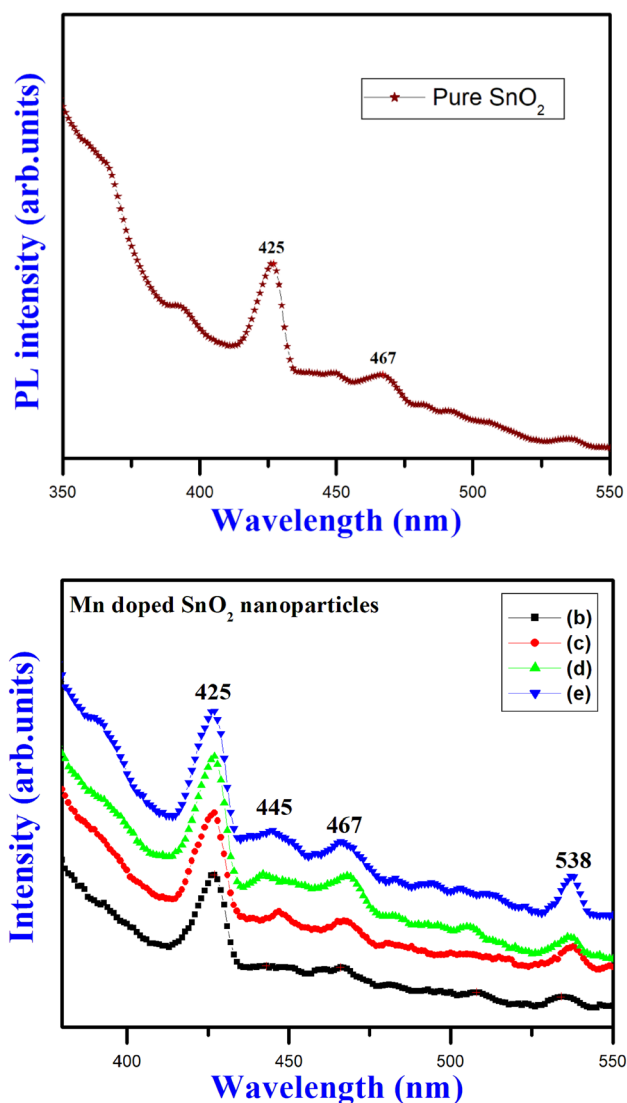
Fig. 8 Photoluminescence spectra of pure SnO_2 (b) 0.015 M%, (c) 0.025 M%, (d) 0.035 M% and (e) 0.045 M% Manganese doped SnO_2 nanoparticles

of Mn^{2+} and Sn^{4+}, thus created give increase to defect levels in the crystal and hence enhance the emissions. Therefore, the show best activity of 0.045 M% manganese doped SnO_2 nanoparticles, due to smaller particle size distribution and larger surface area. From the results, the manganese concentrations play a very important role in modifying the optical properties of the SnO_2 samples.

3.7 Electrochemical properties analysis

Figure 9 shows, that the cyclic voltammetry study of pure and manganese (0.015, 0.025, 0.035 and 0.045 M%) doped SnO_2 electrode was recorded at a different scan bar in 5, 10, 30, 50 and 100 mV/s and all products calcinated at 700 °C. It

reveals that an electrode material combines at the same time two type of energy storage mechanism EDLC with Faradaic capacitance. Which were measured at −0.2 to +0.2 V potential window. The curves of pure and manganese doped SnO_2 nanoparticles exhibit a similar rectangular shape with redox peak, represents the electrodes not only acquire good EDLC but also display obvious pseudocapacitance from manganese doped SnO_2 nanoparticles [43]. The specific capacitances values of the SnO_2 electrode can be computed by using the formula [44].

$$C_S = \frac{Q}{m\Delta v} \qquad (5)$$

where the specific capacitance is Cs (Fg^{-1}), the average charge in the anodic and cathodic scan bar is Q, the mass of the active material is m, and the potential range is ΔV [45]. Electrochemical properties were done in 0.2 M tetra butyl ammonium perchlorate with a normal three electrode configuration comprising of a product is working electrode, an Ag/AgCl as a reference electrode and a platinum wire as a counter electrode [44].

In the present work, pure and manganese doped SnO_2 nanoparticles have different scan bar such as 5, 10, 30, 50 and 100 mV/s. Moreover, pure SnO_2 nanoparticles revealed that the specific capacitance values 156.7 F/g for low scan bar at 5 mV/s. And lower specific capacitance 1.7 F/g was identified for the higher scan bar 100 mV/s, the doping concentrations of Mn increase with increased the specific capacitances. In general, the higher specific capacitance was identified in the manganese (x = 0.045%) doped SnO_2 nanoparticles in which lower scan bar 5 mV/s for increasing the specific capacitance value are 285.2 F/g. Higher scan bar 100 mV/s for decreasing the specific capacitance is 5.6 F/g. From the mechanism of lower scan bar at increasing the specific capacitance due to the electrolyte ions have enough time to penetrate the pores of the material and higher scan bar decreasing behavior of specific capacitance in which only it accumulates on the outer surface. The results were tabulated in Table 2. In addition, the observed specific capacitance esteems were higher than the reported values of the pure and manganese doped SnO_2 synthesized by wet chemical methods [46–48].

Dinesh et al. [49], announced the specific capacitance value of Cd_2SnO_4 nanoparticles by hydrothermal method was 112 F/g. The higher specific capacitance esteem saw in the present study confirms that good crystallinity of the manganese doped SnO_2 nanoparticles.

3.8 Magnetic properties analysis

Figure 10 shows room temperature M–H loop of pure SnO_2 and Mn-doped SnO_2 nanoparticles annealed at 700 °C were recorded with a range of +15 KOe to −15 KOe for the
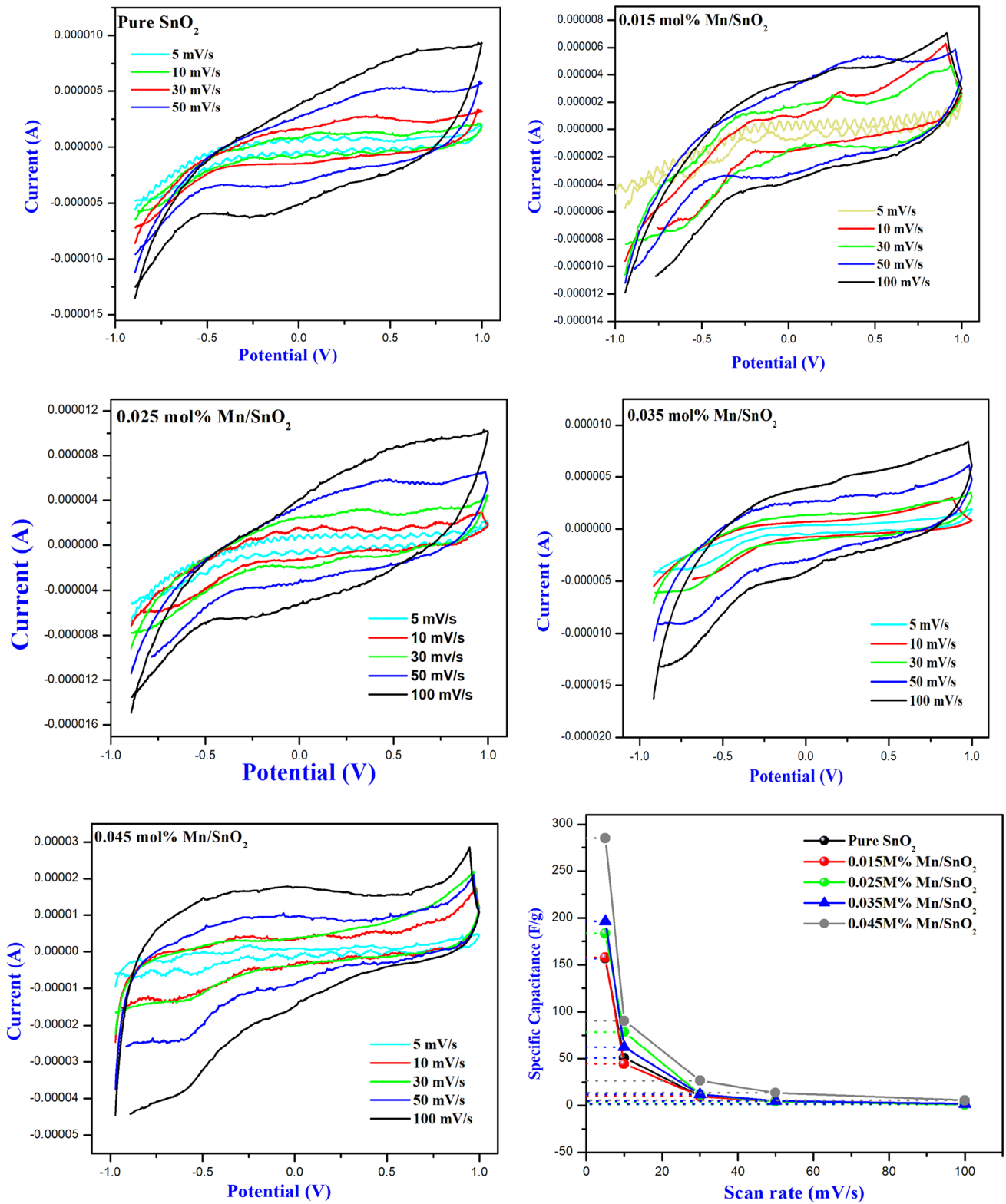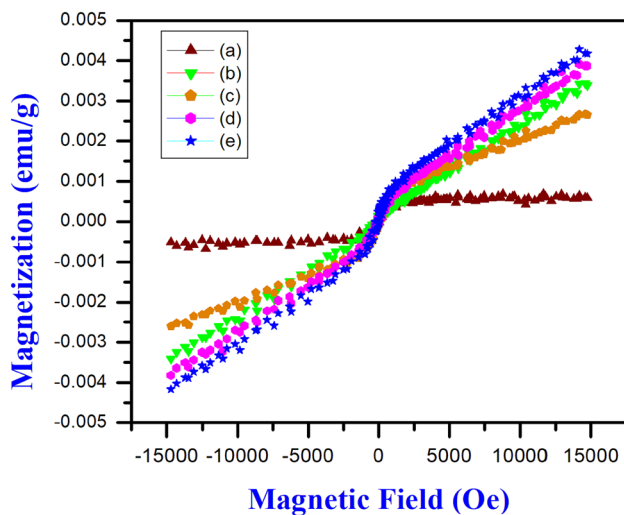
Fig. 9 Cyclic voltammogram of pure and Manganese (0.015, 0.025, 0.035 and 0.045%) doped SnO$_2$ electrode for different scan rates with 700 °C and different scan rates their specific capacitance values

Table 2 The different scan rate and their specific capacitance Value of pure and Mn doped SnO_2 (0.015%, 0.025%, 0.035%, 0.045%) calcined at 700 °C

Scan rate (mV/s)	Specific capacitance (Fg^{-1})				
	Pure SnO_2	Mn/SnO_2 (0.015%)	Mn/SnO_2 (0.025%)	Mn/SnO_2 (0.035%)	Mn/SnO_2 (0.045%)
5	156.7	157.7	183.4	196.5	285.2
10	50.9	44.5	78.5	62.3	90.5
30	10.5	9.9	11.92	11.8	26.6
50	4.9	4.6	4.18	5.1	13.6
100	1.7	1.6	1.3	1.9	5.6

Fig. 10 In-plane hysteresis loop recorded at room temperature for the $Sn_{1-x}Mn_xO_2$ ((a) 0.000, (b) 0.015, (c) 0.025, (d) 0.035, and (e) 0.045 M%) samples

$Sn_{1-x}Mn_xO_2$ (x = 0, 0.015, 0.025, 0.035, and 0.045 mol%). It can be seen that the magnetism of the samples strongly depends on the doping content. For the doping concentration 0.015%, 0.025%, ferromagnetic hysteresis loops are recorded at room temperature, while the loops are superimposed by a paramagnetic behavior, whereas, for the doping concentration 0.035%, the ferromagnetism is either suppressed or disappears; only paramagnetism is found. For the doping concentration 0.045% is observed weak ferromagnetic behavior [50]. It is also to be revealed that the pure SnO_2 sample was measured, the signal was not established, analytical of the diamagnetism of SnO_2 matrix. These results intimate that almost higher manganese doping concentration do not contribute to the arrangement of ferromagnetism, it may be due to the arrangement of manganese clusters as a consequence of decreased Mn–Mn distance, as noted in Mn doped zinc oxide bulk samples and powders [51, 52]. Manganese clusters can be produced with increasing of doping

concentration, which can lead to antiferromagnetic pairing connecting Manganese ions and restrain the ferromagnetic property. This line was reported by Sharma et al. [51]. In this case, it is reasonable to suppose that the antiferromagnetic coupling increase and the ferromagnetic coupling degrade with the increase of Manganese concentration in the $Sn_{1-x}Mn_xO_2$ samples.

Before ascribe the observed room temperature ferromagnetism to be intrinsic, one should rule out the possibility that the impurity phase is responsible for the ferromagnetism, although no second phase was detected by XRD study. It is not complicated to exclude the donation from manganese based oxides because no manganese based oxides are ferromagnetic at room temperature, such as MnO, Mn_2O_3 and MnO_2, the materials are antiferromagnetic with Neel temperatures of 116, 76 and 84 K, respectively. The exception is that Mn_3O_4 and $SnMn_2O_4$ are ferromagnetic nature with consequent Curie temperature of 46 and 53 K [53, 54]. These materials cannot report for the ferromagnetism detected at RT. Moreover, if the manganese connected secondary phase is accountable for the formation of ferromagnetic behavior, an increase in manganese concentration would apparently increase the volume fraction of the secondary phase and matching the ferromagnetic property. However, our outcomes indicate that the ferromagnetism decrease with the increase of Mn concentration. Therefore, the ferromagnetism can be due to the incorporation of manganese ions interested in the SnO_2 lattice.

In the current study, although there appears to be no single theory that can explain the ferromagnetism for all oxide DMSs, an imperfection mediated ferromagnetic model based on Bound Magnetic Polaron (BMP) theory has been predicted theoretically [55] and confirmed experimentally [56] the activation of ferromagnetism in oxide DMSs in a crucial role. In support of occurrence, surface defects have been concerned to be necessary for the age group of ferromagnetic in oxide DMSs [57]. Nevertheless, Okabayashi et al. [58] reported enhanced RTFM in Fe and Mn co-doped SnO_2 synthesized by sol gel method. In our result, the increasing concentration of Mn, saturation magnetization gets increased and then decreased [59]. Thus, a weak ferromagnetic behavior is observed at room temperature when the doping concentration at 0.045%. The results were tabulated in Table 3.

4 Conclusions

In this summary pure and manganese (0.015, 0.025, 0.035, and 0.045 M%) doped SnO_2 nanoparticles using the chemical precipitation method and calcinated at 700 °C. XRD pattern confirms that all the products are good nanocrystallite with tetragonal structure. The average crystallite sizes were observed around 37–11 nm. SEM images clarify that

Table 3 Magnetic parameters i.e. remanent magnetization (M_R), coercive field (H_C) and saturation magnetization (M_S) determined from M–H curves of Mn doped SnO_2 (0.015%, 0.025%, 0.035%, and 0.045%) calcined at 700 °C

Composition of X ($Sn_{1-x} Mn_x O_2$)	VSM of hysteresis parameters		
	H_C (Oe)	M_S (emu/g)	M_R (emu/g)
Pure SnO_2 X = 0.000	142.13	0.748	73.276
X = 0.015	136.93	3.8822	87.604
X = 0.025	69.191	2.665	100.85
X = 0.035	105.27	4.2380	93.702
X = 0.045	59.213	3.4688	41.910

the particles are spherical in shape, and well dispersed spherical morphologies, alongside some accumulated particles, were shown in the HR-TEM images, the average particle size was calculated as 36.8–12.0 nm, these are in excellent concord with the size that has been predictable from the XRD. FTIR analysis confirms that the presence of functional groups is identified. The UV–DRS studies confirm that the band gap energy to be 3.75–3.52 eV. From the CV study confirms that the higher capacitance value of 156.7 F/g for pure SnO_2 nanoparticles. The Manganese (0.045%) doped SnO_2 nanoparticles exhibit higher specific capacitance value such as 285.2 F/g at 5 mV/s than pure and other Manganese doped SnO_2 nanoparticles at the lower scan rate. Even the higher scan rate (0.045%) Manganese doped SnO_2 nanoparticles lead the higher capacitance value (5.6 F/g at 100 mV/s). In addition, it improved specific capacitance are esteemed. The typical room temperature ferromagnetic reaction of the pure and manganese doped material is observed. It is found out, the decreasing crystallite size with increasing manganese concentration tend to materials towards weak ferromagnetic and paramagnetic phase. With the ability to create manganese doped SnO_2 with good magnetization at room temperature. Finally, the scientific applications of pure and manganese doped SnO_2 nanoparticles are to manufacture electrochemical sensors and spintronic devices which are used in a pharmaceutical and biological product with the agreeable.

Compliance with ethical standards

Conflict of interest The authors declare that they have no conflicts of interest concerning this article.

References

1. C. Chi-Hsiu, Y.L. Lee, Appl. Phys. Lett. **91**, 053503 (2007). https://doi.org/10.1063/1.2768311
2. M.A. Walling, J.A. Novak, R.E. Jason, Shepard, Int. J. Mol. Sci. **10**, 441–491 (2009). https://doi.org/10.3390/ijms10020441
3. C.B. Wladimir Marine, B.-L. Su, Chem. Phys. Lett. **438**, 67–71 (2007). https://doi.org/10.1016/j.cplett.2007.02.061
4. V.S. Vaishanv, P.D. Patel, N.G. Patel, Mater. Manuf. Process. **21**, 257–261 (2006). https://doi.org/10.1080/10426910500464511
5. J. Hays, A. Punnoose, R. Baldner, M.H. Engelhard, J. Peloquin, K.M. Reddy, Phys. Rev. B **72**, 075203 (2005). https://doi.org/10.1103/PhysRevB.72.075203
6. Y.W. Heo, J. Kelly, D.P. Norton, A.F. Hebard, S.J. Pearton, J.M. Zavada, L.A. Boatner, Electron. Solid-State Lett. **7**, G309–G312 (2004). https://doi.org/10.1149/1.1814596
7. S.A. Wolf, D.D. Awschalom, R.A. Buhrman, J.M. Daughton, S. Von Molnar, M.L. Roukes, A. Yu Chtchelkanova, D.M. Treger, Science **294**, 1488–1495 (2001). https://doi.org/10.1126/science.1065389
8. K.S. Burch, D.D. Awschalom, D.N. Basov, J. Magn. Magn. Mater. **320**, 3207–3228 (2008). https://doi.org/10.1016/j.jmmm.2008.08.060
9. R. Viswanatha, S. Sapra, S. Sen Gupta, B. Satpati, P.V. Satyam, B.N. Dev, D.D. Sarma, J. Phys. Chem. B **108**, 6303–6310 (2004). https://doi.org/10.1021/jp049960o
10. P. Sharma, A. Gupta, F.J. Owens, A. Inoue, K. Venkat Rao, J. Magneti, Magn. Mater. **282**, 115–121 (2004). https://doi.org/10.1016/j.jmmm.2004.04.028
11. S.B. Ogale, R.J. Choudhary, J.P. Buban, S.E. Lofland, S.R. Shinde, S.N. Kale, V.N. Kulkarni, Phys. Rev. Lett. **91**, 077205 (2003). https://doi.org/10.1103/PhysRevLett.91.077205
12. H. Kimura, T. Fukumura, M. Kawasaki, K. Inaba, T. Hasegawa, H. Koinuma, Appl. Phys. Lett. **80**, 94–96 (2002). https://doi.org/10.1063/1.1430856
13. Z.M. Tian, S.L. Yuan, J.H. He, P. Li, S.Q. Zhang, C.H. Wang, Y.Q. Wang, S.Y. Yin, L. Liu, J. Alloys Compd. **466**, 26–30 (2008). https://doi.org/10.1016/j.jallcom.2007.11.054
14. N.H. Hong, A. Ruyter, W. Prellier, J. Sakai, N.T. Huong, J. Phys. Condens. Matter **17**, 6533 (2005). https://doi.org/10.1103/PhysRevB.75.205206
15. N.H. Hong, J. Sakai, W. Prellier, A. Hassini, J. Phys. Condens. Matter **17**, 1697 (2005). https://doi.org/10.1088/0953-8984/17/10/023
16. C.B. Fitzgerald, M. Venkatesan, L.S. Dorneles, R. Gunning, P. Stamenov, J.M.D. Coey, P.A. Stampe, R.J. Kennedy, E.C. Moreira, U.S. Sias, Phys. Rev. B **74**, 115307 (2006). https://doi.org/10.1103/PhysRevB.74.115307
17. K.H. Gao, Z.Q. Li, X.J. Liu, W. Song, H. Liu, E.Y. Jiang, Solid State Commun. **138**, 175–178 (2006). https://doi.org/10.1016/j.ssc.2006.02.032
18. F. Gu, S.F. Wang, C.F. Song, M.K. Lü, Y.X. Qi, G.J. Zhou, D. Xu, D.R. Yuan, Chem. Phys. Lett. **372**, 451–454 (2003). https://doi.org/10.1016/S0009-2614(03)00440-8
19. H. Jin, Y. Xu, G. Pang, W. Dong, Q. Wan, Y. Sun, S. Feng, Mater. Chem. Phys. **85**, 58–62 (2004). https://doi.org/10.1016/j.matchemphys.2003.12.006

20. F. Séby, M. Potin-Gautier, E. Giffaut, O.F.X. Donard, Geochim. Cosmochim. Acta **65**, 3041–3053 (2001). https://doi.org/10.1016/S0016-7037(01)00645-7

21. C. Xu, J. Tamaki, N. Miura, N. Yamazoe, J. Mater. Sci. **27**, 963–971 (1992). https://doi.org/10.1007/bf01197649

22. H. Bastami, E. Taheri-Nassaj, J. Alloys Compd. **495**, 121–125 (2010). https://doi.org/10.1016/j.jallcom.2010.01.099

23. C. Li, Z. Yu, S. Fang, S. Wu, Y. Gui, R. Chen, J. Phys. Conf. Ser. **152**, 012033 (2009). https://doi.org/10.1088/1742-6596/152/1/012033

24. N.S. Sabri, M.S.M. Deni, A. Zakaria, M.K. Talari, Phys. Procedia **25**, 233–239 (2012). https://doi.org/10.1016/j.phpro.2012.03.077

25. P.K. Sarkar, S. Bhattacharjee, M. Prajapat, A. Roy, RSC Adv. **5**, 105661–105667 (2015). https://doi.org/10.1039/C5RA15581A

26. B. Venugopal, B. Nandan, A. Ayyachamy, V. Balaji, S. Amirthapandian, B.K. Panigrahi, T. Paramasivam, RSC Adv. **4**, 6141–6150 (2014). https://doi.org/10.1039/C3RA46378H

27. B. Karunagaran, R.T. Rajendra Kumar, D. Mangalaraj, S.K. Narayandass, G. Mohan Rao, Cryst. Res. Technol. **37**, 1285–1292 (2002). https://doi.org/10.1002/crat.200290004

28. N.J.S. Kissinger, M. Jayachandran, K. Perumal, C.S. Raja, Bull. Mater. Sci. **30**, 547–551 (2007). https://doi.org/10.1007/s12034-007-0085-7

29. B. Sathyaseelan, K. Senthilnathan, T. Alagesan, R. Jayavel, K. Sivakumar, Mater. Chem. Phys. **124**, 1046–1050 (2010). https://doi.org/10.1016/j.matchemphys.2010.08.029

30. N. Tahir, S.T. Hussain, M. Usman, S.K. Hasanain, A. Mumtaz, Appl. Surf. Sci. **25**, 8506–8510 (2009). https://doi.org/10.1016/j.apsusc.2009.06.003

31. S.K. Pandian, K. Karthik, K. Sureshkumar, N. Victor Jaya, Mater. Manuf. Proc. **27**, 130–134 (2012). https://doi.org/10.1080/10426914.2011.557130

32. K. Anandan, V. Rajendran, Superlattices Microstruct. **85**, 185–197 (2015). https://doi.org/10.1016/j.spmi.2015.05.031

33. P. Rajeshwaran, A. Sivarajan, J. Mater. Sci. Mater. Electron. **26**, 539–546 (2015). https://doi.org/10.1007/s10854-014-2432-y

34. A.S. A.Azam, S.S. Ahmed, A.H. Habib, Naqvi, J. Alloys Compd. **523**, 83–87 (2012). https://doi.org/10.1016/j.jallcom.2012.01.072

35. V. Agrahari, A.K. Tripathi, M.C. Mathpal, A.C. Pandey, S.K. Mishra, R.K. Shukla, A. Agarwal, J. Mater. Sci. Mater. Electron. **26**, 9571–9582 (2015). https://doi.org/10.1007/s10854-015-3620-0

36. S.M. Priya, A. Geetha, K. Ramamurthi, J. Sol-Gel Sci. Technol. **78**, 365–372 (2016). https://doi.org/10.1007/s10971-016-3966-7

37. S.M. Sedghi, Y. Mortazavi, A. Khodadadi, Sens. Actuators B **145**, 7–12 (2010). https://doi.org/10.1016/j.snb.2009.11.002

38. C.M. Liu, X.T. Zu, Q.M. Wei, L.M. Wang, J. Phys. D. Appl. Phys. **39**, 2494 (2006). https://doi.org/10.1088/0022-3727/39/12/004

39. F. Gu, S.F. Wang, M.K. Lu, G.J. Zhou, D. Xu, D.R. Yuan, J. Phys. Chem. B **108**, 8119–8123 (2004). https://doi.org/10.1021/jp036741e

40. M.H. Huang, Y. Wu, H. Feick, N. Tran, E. Weber, P. Yang, Adv. Mater. **13**, 113–116 (2001)

41. Q. Tang, W. Zhou, J. Shen, W. Zhang, L. Kong, Y. Qian, Chem. Commun. **21**, 712–713 (2004). https://doi.org/10.1039/B313387G

42. M.K. Singh, M.C. Mathpal, A. Agarwal, Chem. Phys. Lett. **536**, 87–91 (2012). https://doi.org/10.1016/j.cplett.2012.03.084

43. W. Wang, Wu Lei, T. Yao, X. Xia, W. Huang, Q. Hao, X. Wang, Electrochim. Acta **108**, 118–126 (2013). https://doi.org/10.1016/j.electacta.2013.07.012

44. K. Sathishkumar, N. Shanmugam, N. Kannadasan, S. Cholan, G. Viruthagiri, J. Mater. Sci. Mater. Electron. **26**, 1881–1889 (2015). https://doi.org/10.1007/s10854-014-2624-5

45. S. Nagamuthu, S. Vijayakumar, G. Muralidharan, Dalton Trans. **43**, 17528–17538 (2014). https://doi.org/10.1039/c4dt02287d

46. K.R. Prasad, N. Miura, Electrochem. Commun. **6**, 849–852 (2004). https://doi.org/10.1016/j.elecom.2004.06.009

47. C.C. Hu, C.C. Wang, K.H. Chang, Electrochim. Acta **52**, 2691–2700 (2007). https://doi.org/10.1016/j.electacta.2006.09.026

48. K. Karthikeyan, V. Aravindan, S.B. Lee, I.C. Jang, H.H. Lim, G.J. Park, M. Yoshio, Y.S. Lee, J. Alloys Compd. **504**, 224–227 (2010). https://doi.org/10.1016/j.jallcom.2010.05.097

49. S. Dinesh, M. Anandan, V.K. Premkumar, S. Barathan, G. Sivakumar, N. Anandhan, Mater. Sci. Eng. B **214**, 37–45 (2016). https://doi.org/10.1016/j.mseb.2016.08.006

50. T.R. Cunha, I.M. Costa, R.J.S. Lima, J.G.S. Duque, C.T. Meneses, J. Supercond. Nov. Magn. **26**, 2299–2302 (2013). https://doi.org/10.1007/s10948-012-1479-3

51. P. Sharma, A. Gupta, K.V. Rao, F.J. Owens, R. Ahuja, J.M. Guillen, B. Johansson, G.A. Gehring, Nat. Mater. **2**, 673 (2003). https://doi.org/10.1038/nmat984

52. O.D. Jayakumar, H.G. Salunke, R.M. Kadam, M. Mohapatra, G. Yaswant, S.K. Kulshreshtha, Nanotechnology **17**, 1278 (2006). https://doi.org/10.1088/0957-4484/17/5/020

53. K. Dwight, N. Menyuk, Phys. Rev. **119**, 1470 (1960). https://doi.org/10.1103/PhysRev.119.1470

54. D.G. Wickham, N. Menuyk, K. Dwight, J. Phys. Chem. Solids **20**, 316 (1961). https://doi.org/10.1016/0022-3697(61)90020-8

55. A. Kaminski, S.D. Sarma, Phys. Rev. Lett. **17**, 247202 (2002). https://doi.org/10.1103/PhysRevLett.88.247202

56. P.I. Archer, D.R. Gamelin, J. Appl. Phys. **99**, 08M107 (2006). https://doi.org/10.1063/1.2165790

57. H.S. Hsu, J.C.A. Huang, S.F. Chen, C.P. Liu, Appl. Phys. Lett. **90**, 102506 (2007). https://doi.org/10.1063/1.2711763

58. J. Okabayashi, K. Nomura, S. Kono, Y. Yamada, Jpn. J. Appl. Phys. **51**, 023003–023004 (2012). https://doi.org/10.1143/JJAP.51.023003

59. V. Agrahari, M.C. Mathpal, S. Kumar, M. Kumar, A. Agarwal, J. Mater. Sci. Mater. Electron. **27**, 6020–6029 (2016). https://doi.org/10.1007/s10854-016-4525-2